

# Off-Nadir SFMR Brightness Temperature Measurements in High-Wind Conditions

HEATHER M. HOLBACH

*Center for Ocean–Atmospheric Prediction Studies, and Northern Gulf Institute, Florida State University, Tallahassee, and  
NOAA/AOML/Hurricane Research Division, Miami, Florida*

ERIC W. UHLHORN

*AIR Worldwide, Boston, Massachusetts*

MARK A. BOURASSA

*Department of Earth, Ocean and Atmospheric Science, and Center for Ocean–Atmospheric Prediction Studies,  
Florida State University, Tallahassee, Florida*

(Manuscript received 12 January 2018, in final form 3 July 2018)

## ABSTRACT

Wind and wave-breaking directions are investigated as potential sources of an asymmetry identified in off-nadir remotely sensed measurements of ocean surface brightness temperatures obtained by the Stepped Frequency Microwave Radiometer (SFMR) in high-wind conditions, including in tropical cyclones. Surface wind speed, which dynamically couples the atmosphere and ocean, can be inferred from SFMR ocean surface brightness temperature measurements using a radiative transfer model and an inversion algorithm. The accuracy of the ocean surface brightness temperature to wind speed calibration relies on accurate knowledge of the surface variables that are influencing the ocean surface brightness temperature. Previous studies have identified wind direction signals in horizontally polarized radiometer measurements in low to moderate ( $0\text{--}20\text{ m s}^{-1}$ ) wind conditions over a wide range of incidence angles. This study finds that the azimuthal asymmetry in the off-nadir SFMR brightness temperature measurements is also likely a function of wind direction and extends the results of these previous studies to high-wind conditions. The off-nadir measurements from the SFMR provide critical data for improving the understanding of the relationships between brightness temperature, surface wave–breaking direction, and surface wind vectors at various incidence angles, which is extremely useful for the development of geophysical model functions for instruments like the Hurricane Imaging Radiometer (HIRAD).

## 1. Introduction

Remotely sensed measurements of ocean surface brightness temperature ( $T_B$ ) at microwave wavelengths are commonly used to estimate surface wind speeds over the oceans. As wind speed increases, surface roughness and whitewater coverage (composed of active whitecaps and residual foam that persist after wave breaking) increase, leading to an increase of the ocean surface  $T_B$ . The more direct quantity being measured by remote sensing instruments is emissivity  $\varepsilon$ , which for microwaves is related to  $T_B$  through the equation  $\varepsilon = T_B/T$ , where  $T$  is the

physical temperature of the object. There are many other factors that can influence the ocean surface emissivity or  $T_B$  beyond the wind speed, such as wind direction, sea surface temperature (SST), and directional sea state. The greatest factor that determines the  $T_B$  of the ocean surface is the SST. However, for a given SST, it is the wind speed that primarily drives the changes in the ocean surface  $T_B$  measured by microwave radiometers (Uhlhorn and Black 2003; Petty 2006). The relationship between ocean surface  $T_B$  and wind speed at microwave wavelengths is fairly well understood. However, there is a need for more examination of the relationship between ocean surface  $T_B$  with wind and wave direction, especially at wind speeds greater than  $20\text{ m s}^{-1}$ . This study aims to extend the work of previous radiometer studies that

---

*Corresponding author:* Heather Holbach, heather.holbach@noaa.gov

primarily focused on wind speeds less than  $20 \text{ m s}^{-1}$  to higher wind speeds, including in tropical cyclone conditions, by using data collected by the Stepped Frequency Microwave Radiometer (SFMR).

A series of previous studies made use of data from various configurations of an airborne multipolarization radiometer developed by the National Aeronautics and Space Administration (NASA) Jet Propulsion Laboratory (JPL) known as the Wind Radiometer (WINDRAD) to investigate the sensitivity of microwave measurements of the ocean surface  $T_B$  to wind direction. Yueh et al. (1995) examined 19-GHz WINDRAD measurements collected over a range of incidence angles from  $30^\circ$  to  $80^\circ$  at a 20-m wind speed of  $12 \text{ m s}^{-1}$  to study the azimuthal changes in the  $T_B$  measurements with respect to wind direction. They found that horizontally polarized brightness temperature  $T_h$  measurements peaked when viewed in the crosswind direction, while vertically polarized brightness temperature  $T_v$  measurements peaked in the upwind/downwind direction. Yueh et al. (1999) built upon their earlier results (Yueh et al. 1995) by investigating additional 19- and 37-GHz WINDRAD measurements collected at incidence angles of  $45^\circ$ ,  $55^\circ$ , and  $65^\circ$ . The range of 5-m wind speeds for their data was  $0\text{--}26 \text{ m s}^{-1}$ . Similar to Yueh et al. (1995), this study also revealed that the  $T_h$  peaks align with a crosswind relative look direction and that the  $T_v$  peaks align with an upwind/downwind relative look direction. Finally, Yueh et al. (2006) studied WINDRAD data at 17, 19, and 37 GHz collected in Hurricane Erika (1997) at incidence angles of  $45^\circ$ ,  $55^\circ$ , and  $65^\circ$  with dropwindsonde (dropsonde) surface wind speeds up to  $35 \text{ m s}^{-1}$ . For all of the frequencies in their study, the  $T_h$  and  $T_v$  azimuthal features were overwhelmed by contributions from nonuniform atmospheric attenuation during the flights, which obscured any potential wind direction features present in the data. However, it should be noted that measurements of the third and fourth Stokes parameters were available for those studies and a wind direction dependence was identified in those measurements. The SFMR is linearly polarized and does not have the third and fourth Stokes parameters available. Therefore, the background information included here focuses on the results that apply to  $T_h$  and  $T_v$ .

Wentz (1992) investigated the possibility of obtaining wind direction from the spaceborne Special Sensor Microwave Imager (SSM/I), which operates at frequencies of 19, 22, 37, and 85 GHz. This study identified a wind direction signal present in the  $T_h$  measurements with peaks in the crosswind viewing direction for three wind speed ranges with means of 3.9, 7.9, and  $12.2 \text{ m s}^{-1}$ . Meissner and Wentz (2012) utilized data from the spaceborne WindSat polarimetric microwave radiometer and

SSM/I to further investigate the relationship between wind direction and ocean surface emissivity at wind speeds up to  $18 \text{ m s}^{-1}$ . They found an increase in the ocean surface emissivity when the WindSat observations were in the crosswind direction at horizontal polarization (h-pol). Their study covered incidence angles of  $49^\circ\text{--}56^\circ$  and frequencies of 6.8, 10.7, 18.7, 19.3, 37, and 85.5 GHz.

It is quite difficult to obtain microwave radiometer measurements, especially from space, in regions of high winds to study the wind direction signal identified in these previous studies because of the spatial resolution of the instruments compared to the spatial resolution of some high-wind regions, the high rain rates that often accompany high winds in tropical cyclones, and the lower frequency of occurrence of high wind speeds compared to lower wind speeds. However, the SFMR, which is an airborne C-band radiometer mounted on the NOAA and U.S. Air Force hurricane hunter aircraft, makes it possible to fill the gap in these observations at high wind speeds, including in tropical cyclone conditions, for a wide range of incidence angles. During the 2008 and 2014 Atlantic hurricane seasons and 2015 Ocean Winds winter experiment, specially designed experiments were conducted with the NOAA WP-3D hurricane hunter aircraft to collect off-nadir (high incidence angle) SFMR data in tropical cyclones and winter storms to further study the wind direction signal and to confirm that the harmonic signal is not primarily a function of wave direction. Based on the results from Yueh et al. (1995), where they noted an upwind/downwind asymmetry in the minima of the harmonic signal that they thought may be related to the whitecaps being brighter on the downwind side of the waves than those on the upwind side, it is necessary to investigate potential wave direction impacts further in this study. Another reason that wave direction needs to be considered is that breaking waves, which are the primary source for white-water on the ocean surface, generally occur in the direction of the wind. Therefore, it can be difficult to separate the effects of wind and wave direction, and any dependence on wave-breaking direction needs to be examined in order to accurately attribute asymmetries in off-nadir  $T_B$  measurements to wind direction.

One of the main benefits of using the SFMR for this type of study is that the C-band frequencies and stepped-frequency design utilized by the SFMR allow for better removal of atmospheric emissions than the instruments used in previous studies and can obtain accurate measurements in regions of clouds and heavy precipitation. Another benefit of using the SFMR is that it has a smaller footprint compared to the satellite radiometers, which allows for less diversity of the wind conditions within the footprint.

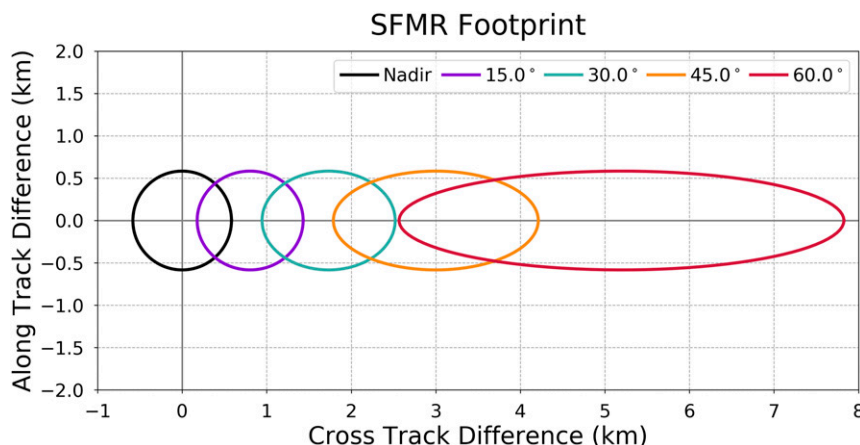


FIG. 1. SFMR footprint size at 3000-m altitude where the along-track and cross-track distances are with respect to the aircraft location and heading. The color of the footprint outlines denotes the incidence angle shown in the top right of the plot.

Improving the understanding of the wind direction signal in microwave measurements at high wind speeds and in tropical cyclones makes it possible to develop more accurate calibrations of  $T_B$  to surface wind speed (and potentially wind direction) over the ocean by satellite microwave radiometers and instruments like the SFMR or the Hurricane Imaging Radiometer (HIRAD; [Amarin et al. 2012](#)), which is designed to obtain a swath of wind speed measurements in tropical cyclones. A brief description of the SFMR will be given in [section 2](#), and the field experiment details and data will be discussed in [section 3](#). [Section 4](#) will present the analysis of the off-nadir SFMR measurements collected in tropical cyclones and winter storms, and show that the wind direction signal is present at higher wind speeds and over a large range of incidence angles. A conclusion will follow in [section 5](#) discussing the implications of the wind direction signal identified in the SFMR off-nadir measurements at high wind speeds and in tropical cyclone conditions.

## 2. Stepped Frequency Microwave Radiometer

The SFMR is a passive, airborne, C-band microwave radiometer designed to measure surface wind speed and rain rate in hurricanes. It was originally developed in 1978 ([Harrington 1980](#)) and has been flown into hurricanes since 1980 ([Jones et al. 1981](#)). Since it was first developed, there have been several iterations on the design of the SFMR, with the most recent version flown for the first time in 2004. The SFMR was considered experimental through 2004 and became operational on the National Oceanic and Atmospheric Administration (NOAA) WP-3D hurricane hunter aircraft in 2005 ([Uhlhorn et al. 2007](#)). It was installed for operations on

the Air Force Reserve Command WC-130J hurricane hunter aircraft in 2008.

The current version of the SFMR operates at six frequencies (4.74, 5.31, 5.57, 6.02, 6.69, and 7.09 GHz) and is designed to obtain surface emissivity measurements, expressed in terms of  $T_B$ , at nadir below the aircraft during level flight. As with changes in altitude, aircraft roll- and pitch- related changes in optical thickness of the atmosphere and polarization of the radiation would impact the retrievals, since the SFMR antenna is fixed to the aircraft. The SFMR footprint size is a function of altitude, and at off-nadir incidence angles, which are examined in this study, the footprint size increases with incidence angle as altitude is held constant ([Fig. 1](#)); however, the solid angle remains the same, conserving the amount of intensity being observed from the surface ([Petty 2006](#)). Therefore, changes in the  $T_B$  measured by the SFMR at off-nadir incidence angles are not related to changes in the geometry of the SFMR footprint, assuming the surface characteristics are homogenous over the footprint. In rain-free conditions this is a good assumption.

Under high-wind conditions, the primary change in the ocean surface  $T_B$  is from the change in the fractional coverage of whitecaps and foam on the ocean surface generated by breaking waves ([Nordberg et al. 1971](#); [Rosenkranz and Staelin 1972](#)). In general, the coverage of whitecaps and foam on the ocean surface and small-scale surface roughness increases as wind speed increases, resulting in an increase in the  $T_B$  measured by a microwave radiometer ([Hollinger 1971](#); [Ross and Cardone 1974](#); [Webster et al. 1976](#); [Swift et al. 1984](#); [Tanner et al. 1987](#)). The effects of whitecaps and foam dominate at high wind speeds. This relationship between whitecapping and foam on the ocean surface

with increasing surface wind speed allows the SFMR to obtain accurate surface wind speed measurements at wind speeds above about  $10 \text{ m s}^{-1}$  (below  $10 \text{ m s}^{-1}$  there is insufficient whitecapping and foam) through category 5 hurricane wind speeds of greater than  $70 \text{ m s}^{-1}$ . However, it should be noted that at off-nadir incidence angles, small-scale surface roughness will have a larger impact than at nadir for h-pol observations. To obtain surface wind speed measurements from the SFMR-measured  $T_B$ , a forward radiative transfer model is implemented to compute a modeled  $T_B$  and an inversion algorithm minimizes the differences between the observed and modeled  $T_B$  to solve for wind speed and rain rate (Uhlhorn and Black 2003; Uhlhorn et al. 2007; Klotz and Uhlhorn 2014).

### 3. Field experiment and data

Data for this study were collected as part of the NOAA/Atlantic Oceanographic and Meteorological Laboratory (AOML)/Hurricane Research Division's (HRD) Hurricane Field Program in 2008 and 2014, and the NOAA 2015 Ocean Winds winter experiment. To obtain off-nadir incidence angle measurements with the SFMR, which has a fixed mounting that points straight down at the surface (nadir) when the aircraft is level, the aircraft must roll at a constant angle (Fig. 2). Therefore, a special experiment was designed to collect SFMR data at off-nadir incidence angles with the NOAA WP-3Ds in tropical cyclones. The SFMR antenna is linearly polarized at nadir and in its operational configuration. However, the antenna will measure more horizontally polarized radiation when the aircraft rolls and more vertically polarized radiation when pitching it.

The SFMR high incidence angle measurements experiment includes collecting SFMR data at several different specified incidence angles (specifically aircraft roll angles) over a minimum of three consecutive circles in rain-free conditions for a wide range of wind speeds (Gamache et al. 2008; Reasor et al. 2014). The primary incidence angles flown in the tropical cyclones that this study investigates are  $15^\circ$ ,  $30^\circ$ , and  $45^\circ$ . This experiment was designed to be flown in rain-free conditions to remove the additional contributions that rain may have on the off-nadir measurements, but the impact of rain will be investigated in a future study. It was also specified that constant incidence (roll) and pitch angles be maintained to reduce noise in the measurements that may be associated with changes in incidence angle or mixing of polarizations that would result from varying the pitch angle. To have a surface wind measurement to compare the SFMR measurements with, a dropsonde was released at the beginning or end of the circles. An

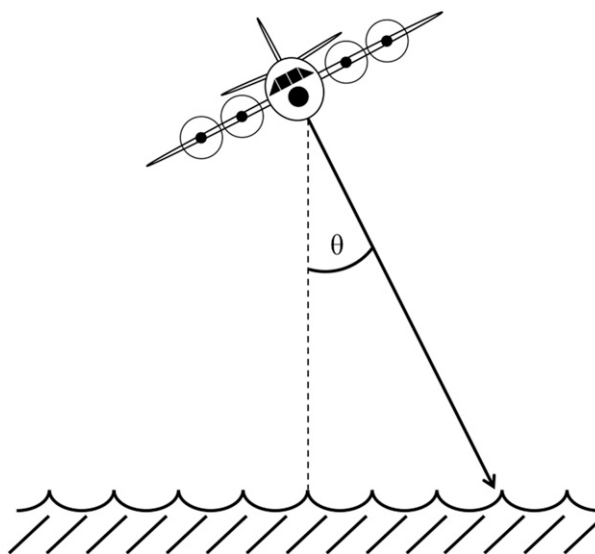


FIG. 2. Schematic depicting the Earth incidence angle for the center of the SFMR footprint (solid line) with respect to nadir (dashed line).

airborne expendable bathythermograph (AXBT) was also released at the beginning or end of the circles to obtain an SST measurement for input to the SFMR radiative transfer model. The data that were collected in tropical cyclones are summarized in Table 1, which includes the storm name, date, dropsonde surface-adjusted wind speed, and incidence angles flown for each flight. The storm-relative locations for the data listed in Table 1 are shown in Fig. 3. Most of the data are located on the right motion-relative side of the storms.

To supplement the off-nadir data collected in tropical cyclones, data from the NOAA 2015 Ocean Winds winter experiment are also used. During the missions for this experiment, data were collected by the SFMR at incidence angles ranging from  $10^\circ$  to  $60^\circ$  in the northern Atlantic Ocean off the coast of Nova Scotia, Canada (Fig. 4), using a similar procedure as the tropical cyclone SFMR high incidence angle measurements experiment design. It should be noted that these cases were collected at many different times of day and not all in daylight. The variety and quantity of incidence angles flown in these missions provided an opportunity to examine the relationship between wind and wave direction and the off-nadir SFMR measurements in further detail than just using the tropical cyclone off-nadir SFMR measurements alone. While the environmental conditions and SSTs that the winter data were collected in are different from those in the tropical cyclone environment, interactions between the wind and wave direction at the ocean surface are still present and will help

TABLE 1. Summary of the tropical cyclone off-nadir SFMR flight data. Boldface incidence angles indicate the cases that passed the quality control checks. The dropsonde surface-adjusted wind speed is given for a single dropsonde released in conjunction with the off-nadir data collection.

Storm	Date	Dropsonde surface-adjusted wind speed ( $\text{m s}^{-1}$ )	Incidence angles ( $^{\circ}$ )
Tropical Storm Dolly	20 Jul 2008	15.4	30, <b>45</b>
Hurricane Gustav	31 Aug 2008	35.2	<b>30, 45</b>
Hurricane Bertha	4 Aug 2014	22.3	15, 30, 45
Hurricane Cristobal	24 Aug 2014	15.1	<b>15, 30, 45</b>
Hurricane Cristobal	25 Aug 2014	27.9	<b>15, 30, 45</b>
Hurricane Cristobal	26 Aug 2014	17.7	<b>30, 45</b>
Hurricane Gonzalo	15 Oct 2014	23.2 (SFMR estimate)	20
Hurricane Gonzalo	16 Oct 2014	36.0	30, 45
Hurricane Gonzalo	17 Oct 2014	40.5	30, 45

improve the understanding of the effect of wind and wave direction on the SFMR measurements. Table 2 summarizes the date, dropsonde surface-adjusted wind speed, and incidence angles for the data from the winter flights.

#### a. Dropsondes

A dropsonde is an airborne expendable instrument that is launched through a chute in the hurricane hunter aircraft. It obtains measurements of pressure, temperature, and humidity at a sampling rate of 2 Hz along with wind speed and wind direction at a sampling rate of 4 Hz (updated from 2 Hz in 2010) from when it is launched from the aircraft until it reaches the ocean surface (Hock and Franklin 1999; Vaisala 2014). The raw dropsonde

files used in this study are provided by NOAA/AOML/HRD and are analyzed using the Earth Observing Laboratory (EOL) Atmospheric Sounding Processing Environment (ASPEN; Martin 2007) software.

The dropsonde wind speed utilized in this study is the layer mean wind speed for the lowest 150 m (WL150). The benefit of using the WL150 wind speed adjusted to the surface is that dropsondes may not always obtain measurements all the way to the surface. If they do, the instantaneous dropsonde surface wind speed measurement may contain more variability in the wind partially related to the nature of the semi-Lagrangian measurement and thus an adjusted layer mean wind speed should be more representative of the 1-min average 10-m wind speed than the instantaneous dropsonde surface wind speed measurement (Uhlhorn et al. 2007). The WL150 wind speeds are adjusted to the surface by multiplying the WL150 wind speed by the ratio  $r(z)$  of the dropsonde

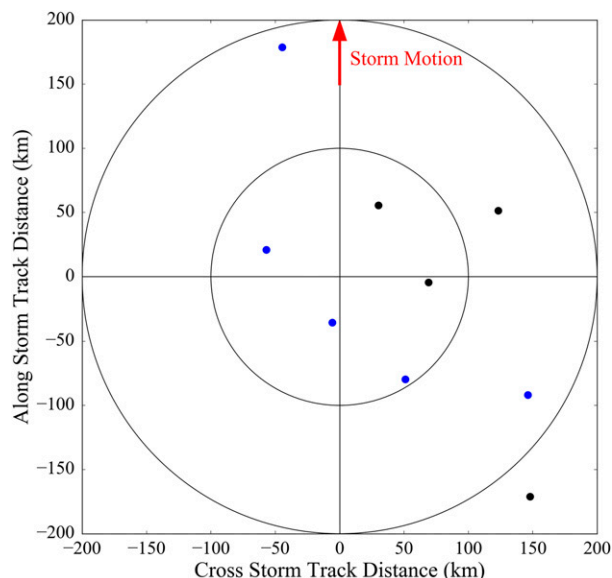


FIG. 3. Storm-relative locations of the circles flown to collect SFMR data for this study. Blue dots indicate the cases that pass the quality control checks. Storm motion (red arrow) is indicated as being toward the top of the plot.

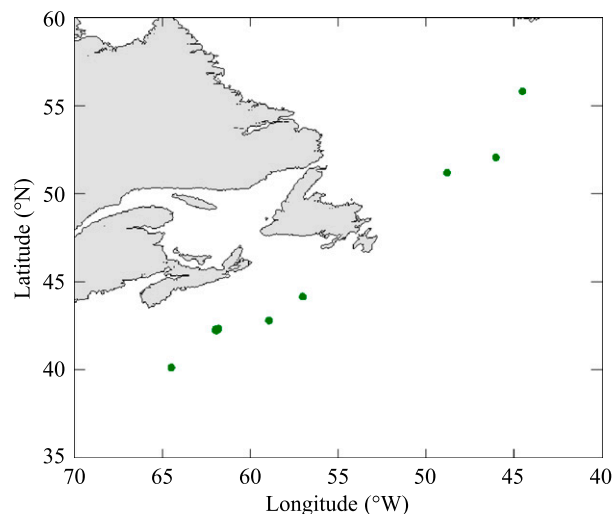


FIG. 4. SFMR off-nadir incidence angle data collection locations (green dots) for the 2015 NOAA Ocean Winds winter experiment.



TABLE 2. Summary of the off-nadir SFMR flight data from the NOAA 2015 Ocean Winds winter experiment. Boldface incidence angles indicate the cases that passed the quality control checks. The dropsonde surface-adjusted wind speed is given for a single dropsonde or a range of wind speeds if multiple dropsondes were released in conjunction with the off-nadir data collection.

Date	Dropsonde surface-adjusted wind speed ( $\text{m s}^{-1}$ )	Incidence angles ( $^{\circ}$ )
15 Jan 2015	13.7	<b>10, 20, 30, 40</b> , 50, 60
16 Jan 2015	11.54	<b>10</b> , 20, 30, 40, 50, 60
18 Jan 2015	26.6	<b>10, 20, 25, 30, 35, 40, 45, 50</b>
20 Jan 2015	11.95, 12.2	10, 20, 30, 40, 50, 60
23 Jan 2015	18.34–20.5	<b>10, 20, 25, 30, 35, 40, 45, 50</b> , 55, 60
25 Jan 2015	25.4–28.72	<b>10, 30, 50, 60</b>
29 Jan 2015	7.47–8.13	10, 20, 30, 40, 50, 60
31 Jan 2015	8.22–8.88	10, 20, 30, 40, 50, 60
1 Feb 2015	14.28–17.6	<b>10, 20, 30, 40</b> , 50, 60
5 Feb 2015	12.95–14.28	<b>25, 40</b>
8 Feb 2015	16.77–17.68	<b>25, 40</b>
11 Feb 2015	18.09–23.16	<b>25, 40</b>
12 Feb 2015	8.88–15.94	<b>25, 40</b>

near-surface wind speed to the WL150 wind speed corresponding to the lowest 150-m-average wind speed, where  $z$  is the mean altitude of the layer. This ratio is given in functional form by [Uhlhorn et al. \(2007\)](#) and was developed using the mean eyewall profile given by [Franklin et al. \(2003\)](#),

$$r(z) = 1.0314 - 4.071 \times 10^{-3}z + 2.465 \times 10^{-5}z^2 - 5.445 \times 10^{-8}z^3. \quad (1)$$

The resulting adjusted surface wind speed is used as the comparison wind speed measurement for the SFMR  $T_B$  data. Since this adjustment was developed using hurricane eyewall dropsonde profiles, it may not be as accurate for the dropsondes released in the winter storm environment. The roughness lengths might be different from those in the tropical cyclone environment because of changes to the fetch (differences in both distance and duration limits) and hence differences in the development stage of the wave field. While a log wind profile is valid in both of these environments and the effects of stability are minimal at the wind speeds being studied, the changes in the roughness length will result in changes to the log wind profile. These changes would result in systematic errors (biases) in the adjusted wind. However, the dropsonde surface-adjusted wind speeds are used only as a reference for a general comparison between the off-nadir cases and do not impact the SFMR measurements.

The dropsonde measurement of surface wind direction is used to calculate the off-nadir SFMR look direction relative to the surface wind direction. Although the dropsondes obtain only a single-point measurement of the surface wind speed and direction, the assumption is made that the time-averaged surface wind speed and

direction in the region sampled during the circle flights is homogenous.

#### b. Wave directions

The initial plan for identifying the wave direction at the location of the off-nadir SFMR measurements was to use wave spectra data obtained by the NOAA Wide-Swath Radar Altimeter (WSRA; [Walsh et al. 2014](#)). However, the WSRA was not available during the flights that the off-nadir SFMR data were collected. Therefore, the primary observational method available for obtaining surface wave directions was from videos created by the downward-pointing camera mounted on the WP-3D aircraft. When viewing the videos, it is possible to track the arc-shaped active whitecaps from breaking waves between frames and to determine the wave-breaking direction with respect to the video orientation ([Fig. 5](#)). Since the wave-tracking method is dependent upon wave breaking, the primary wave directions will be those of wind waves, but they could also be those of young swell. It is also possible to identify the direction of mature swell in some cases ([Fig. 5b](#)). After determining the direction of the breaking waves with respect to the video orientation, the Earth-relative wave-breaking direction can be determined with knowledge of the camera mounting with respect to the aircraft heading at the time of the video frame. An obvious drawback to this method is that it is not possible to see the ocean surface when there are clouds between the aircraft and the ocean surface obstructing the view or at night. The wave-breaking directions obtained from the aircraft video are also compared with visual observations from scientists on board the aircraft, if available. Another resource for comparing wave-breaking directions for the tropical storm flights from aircraft video are

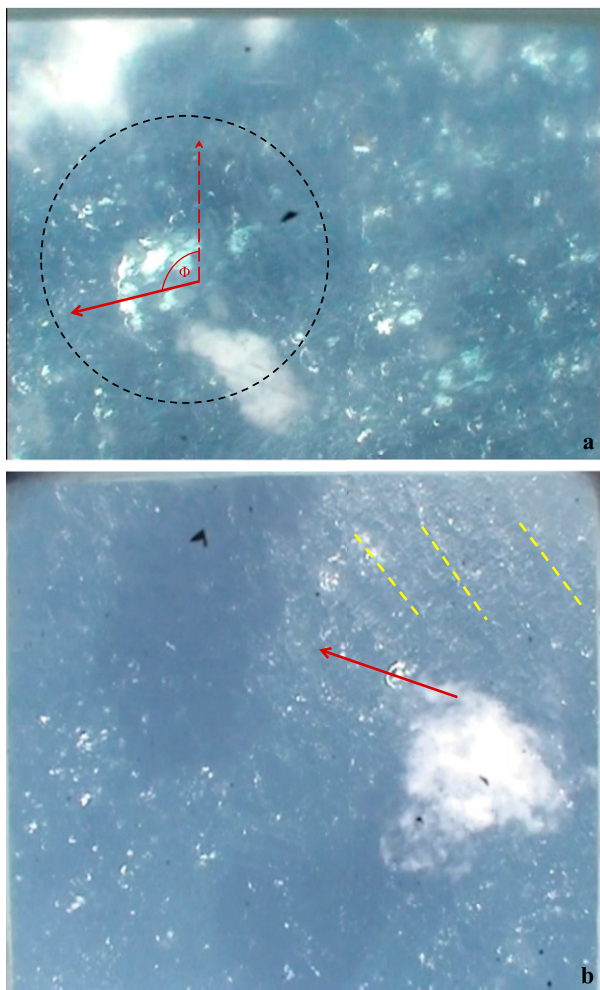


FIG. 5. (a) Video screen shot from the downward-pointing camera at 2018:29 UTC 25 Aug during the flight into Hurricane Cristobal (2014) on NOAA43. The solid red arrow denotes the direction of breaking waves, while the dashed red arrow denotes the direction the aircraft was traveling;  $\phi$  is the angle between the wave-breaking direction and the aircraft heading that is used to determine the Earth-relative wave direction. For reference, the black dashed circle denotes the approximate half-power footprint for the 4.74-GHz SFMR channel. (b) Video screen shot from the downward-pointing camera at 1653:30 UTC 16 Jan 2015 from the winter flight on NOAA42. The solid red arrow denotes the direction of wave breaking, while the yellow dashed lines denote the swell peaks observed in the presence of sun glint.

previous hurricane wave spectra studies (Wright et al. 2001; Elachi et al. 1977; Pore 1957; Holt and Gonzalez 1986; King and Shemdin 1978). Unfortunately, aircraft videos are not available for the 2008 hurricane season. Therefore, wave-breaking directions are not obtained for Tropical Storm Dolly (2008) and Hurricane Gustav (2008).

The aircraft video wave-breaking directions for the winter off-nadir SFMR data are also compared with wave directions from WAVEWATCH III (WW3;

Chawla et al. 2013). WW3 was developed at the National Centers for Environmental Prediction (NCEP) and is a third-generation spectral wave model. NCEP maintains a historical archive of wave hindcasts from WW3 that are forced by NCEP Global Forecast System (GFS) analysis winds. The hindcasts are provided for several different domains and grid spacings. For this study, the global 30-arc-min, or  $\frac{1}{2}^{\circ} \times \frac{1}{2}^{\circ}$ , gridded partitioned dataset is chosen and it has a temporal spacing of 1 h. The partitioned dataset separates the 2D wave spectra by identifying different peaks in the spectrum and classifies them as wind seas or swell using an inverse wave age criteria. Note that the partitioned data are output at every other grid point on the global grid. This dataset provides 10-m wind speeds and wind direction from the GFS, significant wave height, peak period, mean wave direction at the peak period, wavelength at the peak period, and the wind sea fraction, where 1 signifies wind seas and 0 signifies swells, of the partition.

As a first check on the WW3 data, the GFS surface winds are compared to the aircraft flight-level winds and dropsonde winds, scatterometer winds, and buoy winds if available. After verifying the WW3 GFS winds, the WW3 peak wave direction for partitions with wave fractions greater than 0.6 (closer to wind seas than swell, as wave breaking is associated with wind seas) is compared to the visual observations from the aircraft videos. In some cases, there can be some variation in the observations of the aircraft video wave-breaking direction. This can occur for several reasons: 1) the video observations have an error associated with the visual determination of the wave propagation, since the direction of propagation is being estimated by the human eye; and 2) the wave directions determined from video observations made while the aircraft is turning can be different within a few seconds of each other because the aircraft's heading is changing as it turns. Therefore, if the WW3 peak wave direction is in good agreement (within  $\pm 30^{\circ}$ ) with most of the video wave direction observations, then the average WW3 peak wave direction over a region encompassing the aircraft turns is used. For the winter cases that had aircraft video wave directions available, the WW3 peak wave is, for the most part, in very good agreement with the video observations. Therefore, the average WW3 peak wave direction for the region encompassing the aircraft turns is used as the reference wave direction for the winter cases.

### c. Data quality control

As part of the quality control of the tropical cyclone off-nadir SFMR measurements, the WP-3D lower fuselage radar data, provided by HRD, are used to check for precipitation. The lower fuselage radar is a C-band

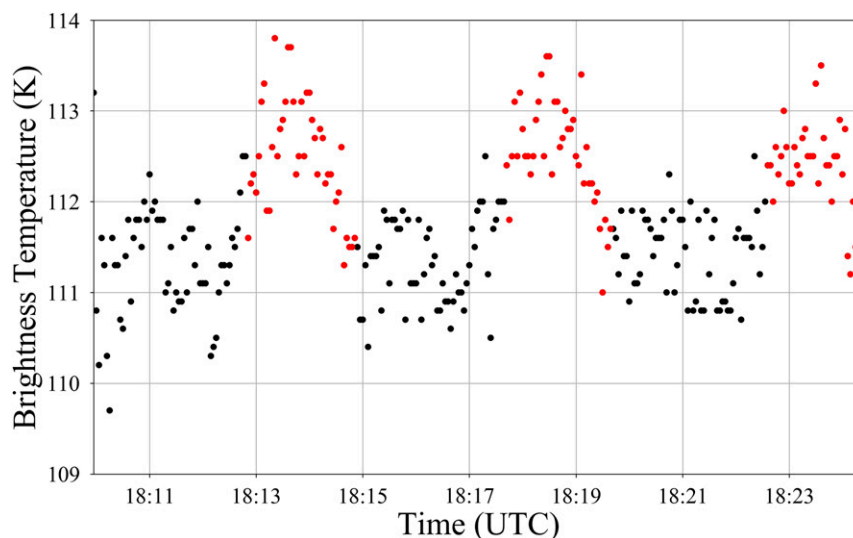


FIG. 6. Brightness temperature time series from the 4.74-GHz channel for the 15° circles in the low-wind flight on 11 Sep 2014. Red dots indicate the time periods where sun glint was in the field of view of the aircraft video.

radar mounted on the underside of the aircraft that scans horizontally (Jorgensen 1984). After the tropical cyclone off-nadir SFMR data are quality controlled for precipitation, several flight-level variables are also inspected. The flight-level variables analyzed include the aircraft roll angle to identify its consistency throughout the data collection for each flight along with the pitch and altitude of the aircraft to determine the vertical stability of the aircraft during the circles. The thresholds used for quality controlling the data include the aircraft roll and pitch angles varying by less than  $\pm 2^\circ$  and the altitude varying by less than  $\pm 50$  m. It is very important that the aircraft is vertically stable during the circles to reduce the mixing of polarizations that could impact the conclusions of this research. Also of note, the SFMR on the WP-3D aircraft are mounted angled slightly down to account for the typical aircraft in-flight pitch, which also helps to reduce the mixing of polarizations during the circles.

Another feature that is quality controlled for in the tropical cyclone off-nadir SFMR data is the presence of sun glint, which is the specular reflection of sunlight from the ocean surface. The sun is very hot at microwave frequencies, especially at those used by the SFMR, and sun glint has been shown to impact microwave  $T_B$  measurements of the ocean surface, particularly at h-pol (Wentz 1981). The presence of sun glint during the circles can be seen in the aircraft downward-pointing videos that are used for identifying the wave-breaking directions. With the help of the aircraft videos, it is possible to note the times during the circles that the sun glint is maximized in the field of view of the SFMR. For the 15° circles, the sun glint is in the field of view of the

camera for about  $\pm 60$  s of the maximum time. For the 30° circles, this time range is about  $\pm 20$  s and for the 45° circles about  $\pm 13$  s. The impact of the sun glint will vary with sun angle, latitude, time of year, and incidence angle; however, this study is focused only on the presence of sun glint, not the magnitude. Time series of the SFMR  $T_B$  identify changes in the  $T_B$  during the times noted from the videos. With the aid of two low-wind flights that occurred on 11 and 17 September 2014 with data collected at off-nadir incidence angles, an increase in the SFMR-measured  $T_B$  is seen clearly when sun glint is present in the SFMR field of view during the circles (Fig. 6). Because these flights on 11 and 17 September occurred in regions with surface wind speeds less than  $5 \text{ m s}^{-1}$ , the changes in the  $T_B$  can be attributed to a feature other than wind. Any measurements obtained in regions where sun glint was present are not used. The bold incidence angles in Table 1 indicate the final tropical cyclone cases that remain to be used in this study for analysis of the off-nadir asymmetry after the quality control.

The winter off-nadir SFMR data are quality controlled in a similar fashion as the tropical cyclone off-nadir SFMR data except that no lower fuselage radar data are available for the winter flights. The aircraft videos are used as a way to check for precipitation in these cases when available. Since the majority of the systems that the winter data were collected in were midlatitude cyclones, precipitation is typically not as abundant, which is one of the reasons why the lower fuselage radar was not used during the flights. Several circles are eliminated from the winter data because of



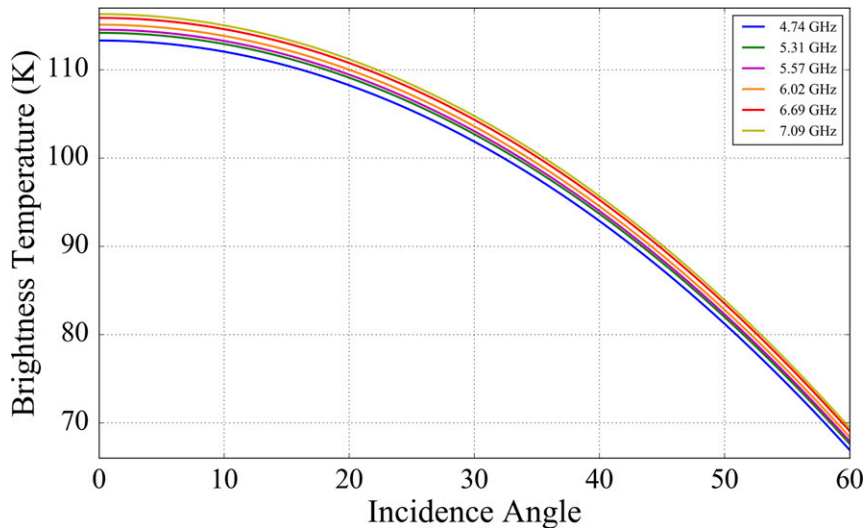


FIG. 7. Brightness temperature relationship with incidence angle for zero wind speed and rain-rate conditions computed using the Klein and Swift (1977) algorithm with typical values of the input variables (SST = 28.0°C, salinity = 36.0 ppt, altitude = 3000 m, ambient temperature = 10.0°C). Line colors correspond to the frequencies noted in the legend.

large fluctuations in pitch angle and altitude along with the presence of sun glint. Many of the cases removed are those at the higher incidence angles of 50° or greater where it is difficult for the pilots to maintain the roll angle, pitch angle, and altitude. For the winter flights, the 5.31-GHz channel is removed from the analysis because of interference from an active remote sensing instrument mounted on the aircraft operating at a similar frequency. The remaining winter off-nadir SFMR data that will be considered for further analysis are indicated by the bold incidence angles in Table 2.

#### 4. Wind-induced brightness temperature

After the data are quality controlled, the off-nadir SFMR  $T_B$  measurements are analyzed by computing the wind-induced component of the ocean surface  $T_B$ . It is important to remember that the  $T_B$  measured by the SFMR  $T_{B_{\text{sfmr}}}$  is the apparent brightness temperature of the scene below the aircraft to the ocean surface. To understand how the  $T_B$  measurements are influenced by changes in the surface characteristics from wind and waves at off-nadir incidence angles, it is necessary to remove the components of the  $T_B$  that are associated with the atmospheric  $T_{Ba}$  and cosmic radiation  $T_{B_{\text{cos}}}$ , as well as the smooth (specular) ocean surface brightness temperature  $T_{B0}$ . The wind-induced brightness temperature  $T_{Bw}$  is defined as

$$T_{Bw} = T_{B_{\text{sfmr}}} - T_{B0} - T_{Ba} - T_{B_{\text{cos}}}. \quad (2)$$

The calculation of  $T_{Ba}$  is adjusted to account for the change in the pathlength through the atmosphere at off-nadir incidence angles, which does not result in a large change to the calculation. The value of  $T_{B0}$  is computed using the Klein and Swift (1977) algorithm, and an example of how it varies with incidence angle for typical values of the input variables (SST = 28.0°C, salinity = 36.0 ppt, altitude = 3000 m, ambient temperature = 10.0°C) is provided in Fig. 7. Accounting for the dependence on incidence angle in the calculation of  $T_{B0}$  removes up to 3000 (or ~3%)  $T_B$  errors that would be present in the  $\pm 2^\circ$  roll angle window. Any remaining variations in  $T_{Bw}$  should be related to changes from the whitewater coverage in the SFMR field of view.

Figure 8 displays time series of  $T_{Bw}$  for the 25° circles from the 23 January 2015 winter flight and for the 45° circles from the 24 August 2014 flight in Hurricane Cristobal. There is a clear oscillation present in the time series of  $T_{Bw}$ . To determine if this oscillation is truly a function of the wind direction and not the wave-breaking direction, the  $T_{Bw}$  are analyzed as a function of the relative look angle of the SFMR  $\theta_r$  with respect to 1) the wind direction and 2) the wave-breaking direction. To calculate the SFMR relative look angles, the direction that the SFMR is pointing with respect to the aircraft heading (+90° when the aircraft rolls right and -90° when the aircraft rolls left) is subtracted from the wind direction or wave-breaking direction (Fig. 9). For the SFMR relative look angles with respect to the wind direction, a relative look angle of  $\pm 90^\circ$  corresponds to the SFMR look direction pointing crosswind,

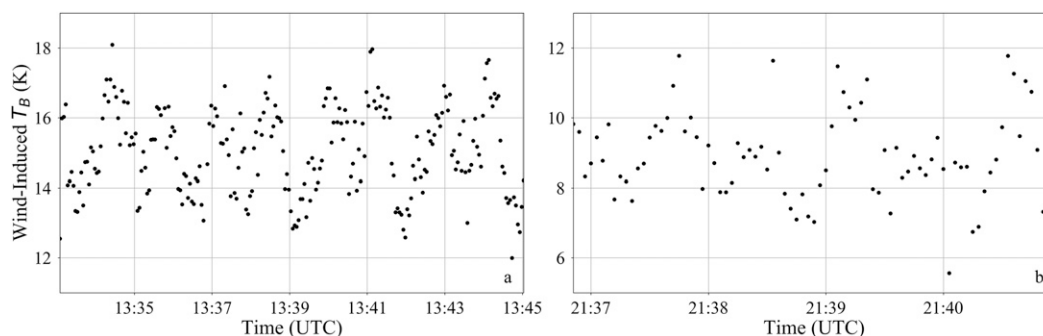


FIG. 8. Time series of the wind-induced brightness temperatures from (a) the 6.02-GHz channel for the 25° circles flown on 23 Jan 2015 and (b) the 7.09-GHz channel for the 45° circles flown on 24 Aug 2014 in Hurricane Cristobal.

0° corresponds to the SFMR look direction pointing downwind, and  $\pm 180^\circ$  corresponds to the SFMR look direction pointing upwind. For the SFMR relative look angles with respect to the wave-breaking direction, a relative look angle of  $\pm 90^\circ$  corresponds to the SFMR viewing perpendicular to the wave-breaking direction, 0° corresponds to the back of the waves aligning with the SFMR look direction, and  $\pm 180^\circ$  corresponds to the front of the waves aligning with the SFMR look direction.

Figure 10 displays the  $T_{Bw}$  shown in Fig. 8 as a function of SFMR relative look angle with respect to both wind (left column) and wave-breaking (right column) direction. It should be noted that the only difference in creating the plots for each case shown is the value for the relative look angle and that the magnitude of the  $T_{Bw}$  are identical (e.g., Figs. 10a and 10b plot the same  $T_{Bw}$ , but the relative look angle for Fig. 10a is with respect to the wind direction and for Fig. 10b it is with respect to the wave-breaking direction). A double harmonic asymmetry is found in the majority of the off-nadir SFMR data for the tropical cyclone and winter cases, which is consistent with previous studies. In most cases, the peaks in the asymmetry align approximately with  $\pm 90^\circ$  (SFMR viewing crosswind or perpendicular to wave-breaking direction).

One of the difficulties with trying to determine if the double harmonic asymmetry in the off-nadir SFMR data is a function of wind direction or wave-breaking direction is that the direction of breaking waves is typically in the direction of the wind (i.e., breaking waves are normally wind waves). However, in high-wind conditions, as the wind direction changes, there can be a lag in the response of the direction of wave breaking, leading to the possibility of differing wind and wave-breaking directions as swell and wind waves interact. Analyzing cases with differing wind and wave-breaking directions can provide insight into the dominant mechanism for the distribution of the whitewater on the ocean surface at

high winds that microwave radiometers respond to when viewing off-nadir. Unfortunately, the difference in the wind and wave-breaking directions in the regions of the TCs sampled in this study is very small. The most likely region of a TC to find differing wind and wave-breaking directions is the rear-left quadrant (Wright et al. 2001), which was the least sampled region for this study. Fortunately, there are two cases in the winter off-nadir SFMR data (8 February and 12 February) that have wind and wave-breaking directions that are different by more than  $30^\circ$ .

In the 8 February case, the wind and wave-breaking directions are different by about  $32^\circ$  and in the 12 February case, the wind and wave-breaking directions are different by about  $38^\circ$ . The GFS wind directions contained within the WW3 output indicate that a shift in the wind direction occurred in the regions where the off-nadir SFMR data were collected, and the GFS wind direction nearest in time agrees with the dropsonde wind directions. This indicates that the scenario described above where the wave-breaking direction lagged a shift in the wind direction was likely valid for these cases. For both of these cases, the peaks of the

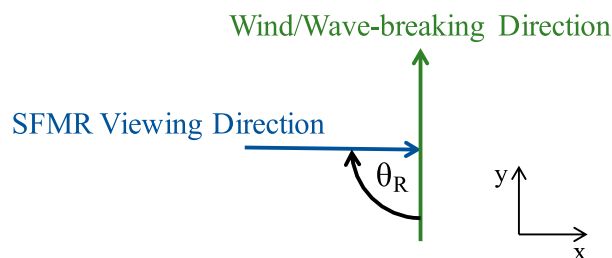


FIG. 9. Schematic depicting the definition of the SFMR relative look angle  $\theta_r$  with respect to wind or wave-breaking direction. The blue arrow depicts the direction the SFMR would be viewing the surface when the aircraft is turning to the left, and the green arrow depicts the wind or wave-breaking direction from a top-down perspective.

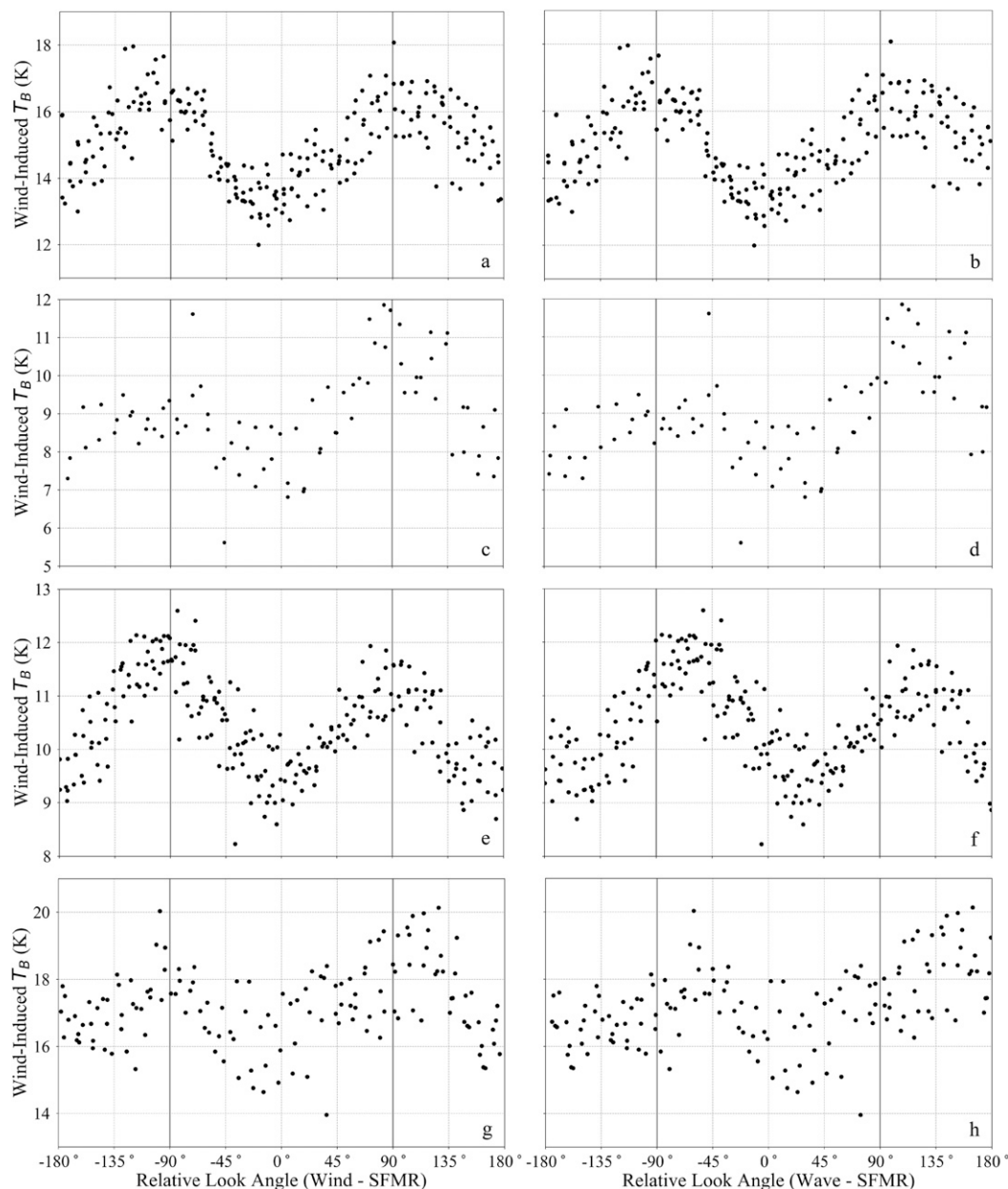


FIG. 10. Wind-induced brightness temperatures plotted as a function of SFMR relative look angle with respect to (left) the wind direction and (right) the wave-breaking direction for the (a),(b) 6.02-GHz channel, 25° circles flown on 23 Jan 2015; (c),(d) 7.09-GHz channel, 45° circles flown on 24 Aug 2014 in Hurricane Cristobal; (e),(f) 4.74-GHz channel, 25° circles flown on 8 Feb 2015; and (g),(h) 6.69-GHz channel, 40° circles flown on 12 Feb 2015. The vertical gray lines emphasize the  $\pm 90^\circ$  relative look angles.

$T_{Bw}$  align with  $\pm 90^\circ$  for the relative look angle with respect to the wind direction (Figs. 10e and 10g) as is seen in the previous cases discussed. However, a shift in the peaks of the  $T_{Bw}$  is observed for the SFMR relative look angle with respect to the wave-breaking direction (Figs. 10f and 10h). The consistency in the location of the peaks of the  $T_{Bw}$  for the relative look angle with respect to the wind direction for all cases examined

leads us to believe that the double harmonic asymmetry is robust to the wind direction and not the wave-breaking direction. However, more data should be collected in coincidence with the WSR to confirm this finding, as the wave directions used for the 8 and 12 February cases are from WW3. Hereafter, the results will be discussed for the SFMR relative look angle with respect to the wind direction.

Physically, the relationship between the relative look angle and the wind direction can be explained by the fact that the wind direction dominates the directional distribution of the whitewater characteristics on the surface. Therefore, when the SFMR views the surface at different angles with respect to the wind direction at off-nadir incidence angles, the changes in the directional distribution of the whitewater characteristics on the surface by the wind direction result in the asymmetry observed in the SFMR measurements. While the wind direction is the dominant signal in this asymmetry, it is possible that a smaller amplitude signal from the wave-breaking direction may also be present as suggested by Yueh et al. (1995), but further data are needed to determine if a wave-breaking signal is present. This finding agrees with the previous studies and shows that the asymmetry related to the wind direction is present at high wind speeds and in extreme environments, such as tropical cyclones.

To quantify the asymmetries in the  $T_{Bw}$ , Fourier series are fit to the  $T_{Bw}$  residuals ( $\Delta T_{Bw} = T_{Bw} - \text{mean } T_{Bw}$ ) using least squares regression and take the form of

$$\Delta T_{Bw} = \sum_{n=0}^3 A_n \cos n(\theta_r + \phi_n), \quad (3)$$

where the  $A$ s and  $\phi$ s are fitted parameters corresponding to the  $n$ th harmonic amplitude and phase angles, respectively. The harmonic fits help to identify the pattern of the asymmetry more clearly. Figure 11 displays a comparison of the harmonic fits between frequencies for each incidence angle flown on 26 August 2014 in Hurricane Cristobal, as well as each incidence angle for the flight on 25 January 2015. When comparing the harmonic fits for the different frequencies, an increase in the  $T_{Bw}$  (not shown) and a slight increase in the residuals with increasing frequency are typically observed. This finding is in agreement with other studies (Meissner and Wentz 2012; Sasaki et al. 1987; Hollinger 1971). In the case of the 10° circles on 25 January, the 5.57-GHz channel has the largest  $T_{Bw}$  residuals, indicating the possibility that the instrument interfering with the 5.31-GHz channel may also be impacting the 5.57-GHz channel, but to a lesser extent. However, there are still asymmetries observed in the winter flight data, so the impacts from the interference appear to be primarily to the overall magnitude of the measurements and not the asymmetry.

For the 60° case, there appears to be a triple harmonic asymmetry; however, this is partially a result of very few data points available for this case. However, it is also possible that the asymmetry disappears at the higher incidence angles (greater than 50°) as a result of the

measurement technique, since the distance over which the data are collected is increasing. As the distance over which the data are collected increases, the changes in the wind field over the region being sampled may mask out the asymmetry. Once again, it should be emphasized that more data are needed to fully understand the asymmetry at high incidence angles and high wind speeds.

Another interesting feature to note related to the asymmetries is that for the tropical cyclone flights, the peaks in the asymmetry do not appear to be equal in magnitude, whereas they are more similar in the winter flights. Some possible physical explanations for the observed uneven peaks are that some other atmospheric phenomena, such as boundary layer rolls, may be influencing the surface wind characteristics over the spatial scale of the sampling pattern, which are not possible to detect given the data available for this study or that the more complicated wave field present in the tropical cyclone environment may have an additional influence on this asymmetry. This possibility of wave effects is consistent with younger seas having a greater impact on stress (Taylor and Yelland 2001; Bourassa 2006 and references therein), and younger seas being much more typical around tropical cyclones than midlatitude storms. More data, particularly wave spectra data, are needed to understand the reason for the uneven peaks.

Figure 12 presents a comparison of the harmonic fits between incidence angles for the 31 August 2008 flight in Hurricane Gustav, the 24 August 2014 flight in Hurricane Cristobal, and the 23 January 2015 winter flight, which are flights that cover many different incidence angles and wind speeds. The residuals of the  $T_{Bw}$  are fairly similar for all incidence angles. Figure 12b and 12c display a slight decrease in the residual of the  $T_{Bw}$  with incidence angle. When analyzing the  $T_{Bw}$ , not just the residual, there is some overlap in the harmonic fits between similar incidence angles (not shown), but typically there is an increase in the  $T_{Bw}$  with increasing incidence angle. The SFMR-measured  $T_B$  decreases with increasing incidence angle because the specular surface  $T_B$  decreases with incidence angle. Therefore, the increase in the  $T_{Bw}$  with incidence angle is likely related to an increase in the total amount of whitewater coverage within the SFMR's field of view with increasing incidence angle. The decrease in the measured  $T_B$  and increase in the  $T_{Bw}$  with incidence angle would need to be accounted for in the algorithm to retrieve accurate wind speed estimates. The results show that the increase in  $T_{Bw}$  with incidence angle and the difference between the peaks and troughs of the harmonic amplitudes could result in  $T_{Bw}$  differences of up to 6 K. For the wind speed ranges measured in this study, this

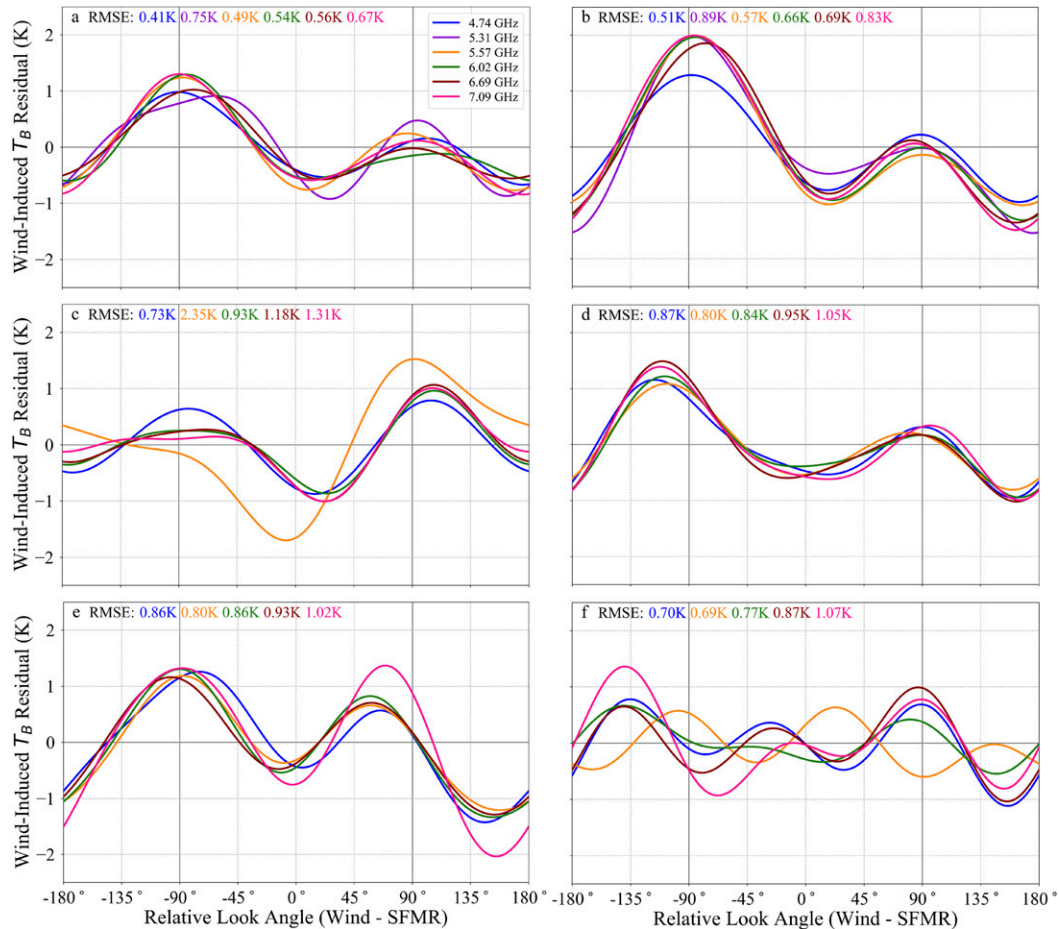


FIG. 11. Harmonic fits to the wind-induced brightness temperature residual vs SFMR relative look angle with respect to the wind direction for (a) 30° and (b) 45° circles flown in Hurricane Cristobal on 26 Aug 2014; and (c) 10°, (d) 30°, (e) 50°, and (f) 60° circles flown on 25 Jan 2015. The line colors correspond to the respective frequencies given by the legend in (a). Root-mean-square error (RMSE) values are also given for the respective fits for each frequency. The vertical gray lines emphasize the  $\pm 90^\circ$  relative look angles.

would correspond to wind speed retrieval errors up to about  $5 \text{ m s}^{-1}$  for the SFMR.

## 5. Conclusions

This study demonstrated that a double harmonic signal was present in off-nadir SFMR measurements, which was determined to be a function of wind direction, in high-wind conditions. This finding of the off-nadir wind direction asymmetry in the SFMR data is a significant contribution to the literature, since the asymmetry has not been shown in h-pol observations at the high wind speeds examined in this study or in tropical cyclone conditions and is further evidence that the wind direction modifies the directional distribution of the whitewater characteristics on the surface viewed by radiometers. The wind direction sensitivity at off-nadir incidence angles indicates that wind direction needs to

be considered when sensing the surface at off nadir to obtain accurate wind speed measurements using instruments like the SFMR.

That the variation in the SFMR  $T_B$  measurements at off-nadir incidence angles was found to be a function of wind direction suggests that this type of technology can be used for obtaining surface wind direction measurements, in addition to wind speed, at incidence angles of about  $15^\circ$  to  $50^\circ$  in high-wind conditions. It may be possible to retrieve wind direction with the SFMR by mounting two units with different polarizations at an off-nadir incidence angle. The effects of wind direction on vertically polarized SFMR measurements is the focus of future work. More work is also needed to quantify the changes in the  $T_B$  measurements at off-nadir incidence angles for h-pol; however, these results help provide more information for retrieval algorithm development to be implemented in newer airborne



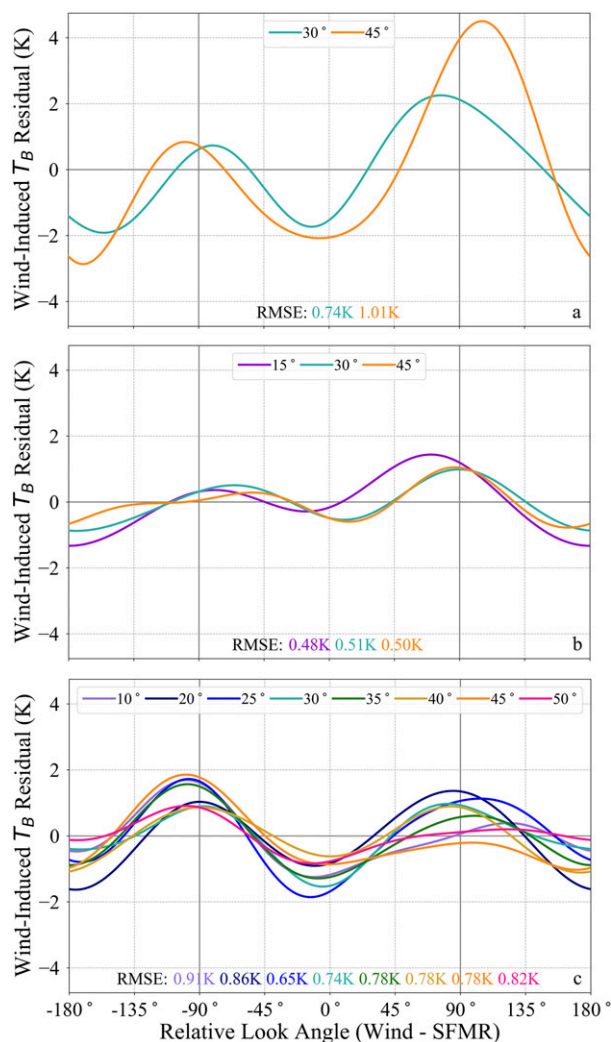


FIG. 12. Harmonic fits to the wind-induced brightness temperature residual vs SFMR relative look angle with respect to the wind direction for the (a) 5.31-GHz channel for the flight in Hurricane Gustav on 31 Aug 2008, (b) the 4.74-GHz channel for the flight in Hurricane Cristobal on 24 Aug 2014, and (c) the 6.69-GHz channel for the winter flight on 23 Jan 2015. The corresponding wind speeds for these flights are 35.2, 15.1, and 19.4  $\text{m s}^{-1}$ , respectively. The line colors correspond to the incidence angles given in the respective legends for each plot. RMSE values are also given for the respective fits for each incidence angle. The vertical gray lines emphasize the  $\pm 90^\circ$  relative look angles.

wind sensing instruments like HIRAD. The results of this study suggest that HIRAD might also be capable of obtaining wind direction measurements given that it obtains measurements at off-nadir incidence angles.

In the future, as more SFMR data are collected, especially in coincidence with the WSRA, the relationships between the directional sea state and wind direction can be quantified further to provide additional understanding of how the wave direction affects the magnitude of the harmonic signal. Improving the

knowledge of this relationship will allow for a better understanding of the physical relationship between wind direction, directional sea state, and surface stress, as well as improve the remotely sensed measurements that are influenced by these relationships. The SFMR provides a unique opportunity to study these relationships in harsh environments like tropical cyclones, which complements the other spaceborne radiometer measurements over the much calmer environments that generally exist over much of the world's oceans. The combination of the airborne and spaceborne radiometer measurements are important for understanding the roles of wind and wave direction on ocean surface  $T_B$  measurements in all weather conditions, which allows for a more complete understanding of the physics over the entire range of wind speeds being measured.

**Acknowledgments.** This work was funded, in part, by the Jet Propulsion Laboratory, National Aeronautics and Space Administration, under Contract 1419699. This work was also funded, in part, by the Northern Gulf Institute (Grants 15-NGI2-105, 15-NGI2-120, and 16-NGI3-01), National Oceanic and Atmospheric Administration, U.S. Department of Commerce, under Awards NA11OAR432019 and NA16OAR4320199. In addition, we thank the amazing pilots and crew at the NOAA Aircraft Operations Center (AOC) for their willingness to collect the SFMR data necessary for this study. We also thank Paul Chang and his group at NOAA NESDIS for their efforts in collecting the off-nadir SFMR data during the Ocean Winds winter experiment. Bradley Klotz and Peter Dodge also provided helpful feedback on the preparation of this manuscript.

## REFERENCES

- Amarin, R. A., W. L. Jones, S. F. El-Nimri, J. W. Johnson, C. S. Ruf, T. L. Miller, and E. Uhlhorn, 2012: Hurricane wind speed measurements in rainy conditions using the airborne Hurricane Imaging Radiometer (HIRAD). *IEEE Trans. Geosci. Remote Sens.*, **50**, 180–192, <https://doi.org/10.1109/TGRS.2011.2161637>.
- Bourassa, M. A., 2006: Satellite-based observations of surface turbulent stress during severe weather. *Atmosphere–Ocean Interactions, Volume 2*, W. Perrie, Ed., WIT Transactions on State of the Art in Science and Engineering, Vol 23, WIT Press, 35–52, <https://doi.org/10.2495/978-1-85312-929-2/02>.
- Chawla, A., and Coauthors, 2013: A multigrid wave forecasting model: A new paradigm in operational wave forecasting. *Wea. Forecasting*, **28**, 1057–1078, <https://doi.org/10.1175/WAF-D-12-00007.1>.
- Elachi, C., T. W. Thompson, and D. King, 1977: Ocean wave patterns under Hurricane Gloria: Observations with an airborne synthetic-aperture radar. *Science*, **198**, 609–610, <https://doi.org/10.1126/science.198.4317.609>.
- Franklin, J. L., M. L. Black, and K. Valde, 2003: GPS dropwindsonde wind profiles in hurricanes and their operational implications. *Wea. Forecasting*, **18**, 32–44, [https://doi.org/10.1175/1520-0434\(2003\)018<0032:GDWPIH>2.0.CO;2](https://doi.org/10.1175/1520-0434(2003)018<0032:GDWPIH>2.0.CO;2).

- Gamache, J., and Coauthors, 2008: 2008 hurricane field program plan. NOAA, 78 pp., <http://www.aoml.noaa.gov/hrd/HFP2008/HFP2008.pdf>.
- Harrington, R. F., 1980: The development of a stepped frequency microwave radiometer and its application to remote sensing of the Earth. NASA Tech. Memo. NASA-TM-81847, 166 pp.
- Hock, T. F., and J. L. Franklin, 1999: The NCAR GPS dropwind-sonde. *Bull. Amer. Meteor. Soc.*, **80**, 407–420, [https://doi.org/10.1175/1520-0477\(1999\)080<0407:TNGD>2.0.CO;2](https://doi.org/10.1175/1520-0477(1999)080<0407:TNGD>2.0.CO;2).
- Hollinger, J. P., 1971: Passive microwave measurements of sea surface roughness. *IEEE Trans. Geosci. Electron.*, **9**, 165–169, <https://doi.org/10.1109/TGE.1971.271489>.
- Holt, B., and F. I. Gonzalez, 1986: SIR-B observations of dominant ocean waves near Hurricane Josephine. *J. Geophys. Res.*, **91**, 8595–8598, <https://doi.org/10.1029/JC091iC07p08595>.
- Jones, W. L., P. G. Black, V. E. Delnore, and C. T. Swift, 1981: Airborne microwave remote-sensing measurements of Hurricane Allen. *Science*, **214**, 274–280, <https://doi.org/10.1126/science.214.4518.274>.
- Jorgensen, D. P., 1984: Mesoscale and convective scale characteristics of nature hurricanes. Part I: General observations by aircraft. *J. Atmos. Sci.*, **41**, 1268–1285, [https://doi.org/10.1175/1520-0469\(1984\)041<1268:MACSCO>2.0.CO;2](https://doi.org/10.1175/1520-0469(1984)041<1268:MACSCO>2.0.CO;2).
- King, D. B., and O. H. Shemdin, 1978: Radar observations of hurricane wave directions. *Coastal Engineering 1978: Proceedings of the Sixteenth International Conference on Coastal Engineering*, ASCE, 209–226, <https://doi.org/10.1061/9780872621909.012>.
- Klein, L. A., and C. T. Swift, 1977: An improved model for the dielectric constant of sea water at microwave frequencies. *IEEE J. Oceanic Eng.*, **2**, 104–111, <https://doi.org/10.1109/JOE.1977.1145319>.
- Klotz, B. W., and E. W. Uhlhorn, 2014: Improved Stepped Frequency Microwave Radiometer tropical cyclone surface winds in heavy precipitation. *J. Atmos. Oceanic Technol.*, **31**, 2392–2408, <https://doi.org/10.1175/JTECH-D-14-00028.1>.
- Martin, C., 2007: ASPEN (Atmospheric Sounding Processing Environment) user manual. NCAR, 56 pp., <https://www.eol.ucar.edu/system/files/Aspen%2520Manual.pdf>.
- Meissner, T., and F. J. Wentz, 2012: The emissivity of the ocean surface between 6 and 90 GHz over a large range of wind speeds and Earth incidence angles. *IEEE Trans. Geosci. Remote Sens.*, **50**, 3004–3026, <https://doi.org/10.1109/TGRS.2011.2179662>.
- Nordberg, W., J. Conaway, D. B. Ross, and T. Wilheit, 1971: Measurements of microwave emission from a foam-covered, wind-driven sea. *J. Atmos. Sci.*, **28**, 429–435, [https://doi.org/10.1175/1520-0469\(1971\)028<0429:MOMEFA>2.0.CO;2](https://doi.org/10.1175/1520-0469(1971)028<0429:MOMEFA>2.0.CO;2).
- Petty, G. W., 2006: Thermal emission. *A First Course in Atmospheric Radiation*, 2nd ed. Sundog Publishing, 113–154.
- Pore, A., 1957: Ocean surface waves produced by some recent hurricanes. *Mon. Wea. Rev.*, **85**, 385–392, [https://doi.org/10.1175/1520-0493\(1957\)085<0385:OSWPBS>2.0.CO;2](https://doi.org/10.1175/1520-0493(1957)085<0385:OSWPBS>2.0.CO;2).
- Reasor, P., and Coauthors, 2014: 2014 hurricane field program plan. NOAA, 116 pp., [http://www.aoml.noaa.gov/hrd/HFP2014/HFP\\_2014.pdf](http://www.aoml.noaa.gov/hrd/HFP2014/HFP_2014.pdf).
- Rosenkranz, P. W., and D. H. Staelin, 1972: Microwave emissivity of sea foam and its effect on nadir radiometric measurements. *J. Geophys. Res.*, **77**, 6528–6538, <https://doi.org/10.1029/JC077i033p06528>.
- Ross, C. B., and V. Cardone, 1974: Observations of oceanic whitecaps and their relation to remote measurements of surface wind speed. *J. Geophys. Res.*, **79**, 444–452, <https://doi.org/10.1029/JC079i003p00444>.
- Sasaki, Y., I. Asanuma, K. Muneyama, G. Naito, and T. Suzuki, 1987: The dependence of sea-surface microwave emission on wind speed, frequency, incidence angle, and polarization over the frequency range from 1 to 40 GHz. *IEEE Trans. Geosci. Remote Sens.*, **GE-25**, 138–146, <https://doi.org/10.1109/TGRS.1987.289813>.
- Swift, C. T., D. C. DeHority, P. G. Black, and J.-Z. Chein, 1984: Microwave remote sensing of ocean surface wind speed and rain rates over tropical storms. *Frontiers of Remote Sensing of the Oceans and Troposphere from Air and Space Platforms: Proceedings of the URSI Commission F Symposium and Workshop*, NASA Conference Publication Series, Vol. 2303, NASA, 281–286.
- Tanner, A. C., C. T. Swift, and P. G. Black, 1987: Operational airborne remote sensing of wind speeds in hurricanes. Preprints, *17th Conf. on Hurricanes and Tropical Meteorology*, Miami, FL, Amer. Meteor. Soc., 385–387.
- Taylor, P. K., and M. J. Yelland, 2001: The dependence of sea surface roughness on the height and steepness of the waves. *J. Phys. Oceanogr.*, **31**, 572–590, [https://doi.org/10.1175/1520-0485\(2001\)031<0572:TDOSSR>2.0.CO;2](https://doi.org/10.1175/1520-0485(2001)031<0572:TDOSSR>2.0.CO;2).
- Uhlhorn, E. W., and P. G. Black, 2003: Verification of remotely sensed sea surface winds in hurricanes. *J. Atmos. Oceanic Technol.*, **20**, 99–116, [https://doi.org/10.1175/1520-0426\(2003\)020<0099:VORSSS>2.0.CO;2](https://doi.org/10.1175/1520-0426(2003)020<0099:VORSSS>2.0.CO;2).
- , —, J. L. Franklin, M. Goodberlet, J. Carswell, and A. S. Goldstein, 2007: Hurricane surface wind measurements from an operational Stepped Frequency Microwave Radiometer. *Mon. Wea. Rev.*, **135**, 3070–3085, <https://doi.org/10.1175/MWR3454.1>.
- Vaisala, 2014: Vaisala dropsonde RD94. Data Sheet, 2 pp. <https://www.vaisala.com/Vaisala%20Documents/Brochures%20and%20Datasheets/RD94-Dropsonde-Datasheet-B210936EN-A-LoRes.pdf>.
- Walsh, E. J., I. PopStefanija, S. Y. Matrosov, J. Zhang, E. Uhlhorn, and B. Klotz, 2014: Airborne rain-rate measurement with a wide-swath radar altimeter. *J. Atmos. Oceanic Technol.*, **31**, 860–875, <https://doi.org/10.1175/JTECH-D-13-00111.1>.
- Webster, W. L. J., T. T. Wilheit, D. B. Ross, and P. Gloersen, 1976: Spectral characteristics of the microwave emission from a wind-driven foam-covered sea. *J. Geophys. Res.*, **81**, 3095–3099, <https://doi.org/10.1029/JC081i018p03095>.
- Wentz, F. J., 1981: The effect of sea-surface sun glitter on microwave radiometer measurements. Remote Sensing Systems Tech. Rep. 110481, 60 pp., <https://ntrs.nasa.gov/archive/nasa/casi.ntrs.nasa.gov/19820018649.pdf>.
- , 1992: Measurement of oceanic wind vector using satellite microwave radiometers. *IEEE Trans. Geosci. Remote Sens.*, **30**, 960–972, <https://doi.org/10.1109/36.175331>.
- Wright, C. W., and Coauthors, 2001: Hurricane directional wave spectrum spatial variation in the open ocean. *J. Phys. Oceanogr.*, **31**, 2472–2488, [https://doi.org/10.1175/1520-0485\(2001\)031<2472:HDWSSV>2.0.CO;2](https://doi.org/10.1175/1520-0485(2001)031<2472:HDWSSV>2.0.CO;2).
- Yueh, S. H., W. J. Wilson, F. K. Li, S. V. Nghiem, and W. B. Ricketts, 1995: Polarimetric measurements of sea surface brightness temperatures using an aircraft K-band radiometer. *IEEE Trans. Geosci. Remote Sens.*, **33**, 85–92, <https://doi.org/10.1109/36.368219>.
- , —, S. J. Dinardo, and F. K. Li, 1999: Polarimetric microwave brightness signatures of ocean wind directions. *IEEE Trans. Geosci. Remote Sens.*, **37**, 949–959, <https://doi.org/10.1109/36.752213>.
- , —, —, and S. V. Hsiao, 2006: Polarimetric microwave wind radiometer model function and retrieval testing for WindSat. *IEEE Trans. Geosci. Remote Sens.*, **44**, 584–596, <https://doi.org/10.1109/TGRS.2005.858416>.